PCCP

Accepted Manuscript

ROYAL SOCIETY OF CHEMISTRY

www.rsc.org/pccp

PCCP

RSCPublishing

PAPER

Excited State Evolution of DNA Stacked Adenines Resolved at the CASPT2//CASSCF/Amber Level: from the Bright to the Excimer State and Back

Cite this: DOI: 10.1039/xoxxoooooox

Received ooth January 2012,
Accepted ooth January 2012

DOI: 10.1039/xoxxoooooox

www.rsc.org/

Irene Conti*[a], Artur Nenov[a], Siegfried Höfinger[b,c], Salvatore Flavio Altavilla[a], Ivan Rivalta[d], Elise Dumont[e], Giorgio Orlandi[a], Marco Garavelli*[a,e]

Deactivation routes of bright ππ* (L_a) and excimer charge transfer (CT) states have been mapped for two stacked quantum mechanical (CASPT2//CASSCF) adenines inside a solvated DNA double strand decamer (poly(dA).poly(dT)) described at the molecular mechanics level. Calculations show that one carbon (C_2) puckering is a common relaxing coordinate for both the L_a and CT paths. By mapping the lowest crossing regions between L_a and CT states, together with the paths connecting the two states, we conclude that at least one CT state can be easily accessible. The lowest-lying conical intersections between ground state (GS) and CT states have been fully characterized in a realistic DNA environment for the first time. We show that the path to reach this crossing region from the CT minima involves high barriers that are not consistent with experimental data lifetimes. Instead, the multiexponential decay recorded in DNA, including the longest (ca. 100 picoseconds) lifetime component detected in oligomeric single- and double-stranded systems, is compatible both with intra-monomer relaxation processes along the L_a deactivation path (involving small barriers) and with population of the excimer (CT) state that is behaving as a trap. In the latter case, deactivation is feasible only going back to the L_a state by following its preferred decay coordinate.

Introduction

Photoinduced events in DNA have always attracted great interest, mainly as ultraviolet light is capable of inducing deleterious strand breaks and mutations[1-5]. The motivation is to understand how the base-surrounding environment changes the decay dynamics of nucleobases. Thanks to experiments and computational studies, the excited state photophysics of the monomer nucleoobases is well understood nowadays. Two life times, τ_1 and τ_2, in the order of hundreds of femtoseconds (fs) to a few picoseconds (ps), characterize monomers lifetimes[6-9]. On the contrary, the photophysics of nucleobase multimers reveals remarkably different features: (i) deactivation occurs over a wider range of time scales[10-16] (in addition to τ_1 and τ_2, a longer lifetime component τ_3, in the order of tens to hundreds ps, appears) and (ii) a long-lived and red-shifted emission is observed [9, 17-21], even if multimers are not significantly more fluorescent than the monomers[9, 19, 22]. The nature of these phenomena is still debated. Due to the increased complexity and variety of possibilities, theoretical analysis is fundamental for deciphering experimental observations.

The seminal works by Kohler and co-workers, applying fs transient-absorption techniques, support a model in which DNA multimers excitations decay to excimeric states, thus accounting for the long lived excited states[1, 3, 10, 12, 16, 23-33]. They indicate that excited states localized on just two stacked bases are the common traps of stacked poly-nucleotides; the fraction of oligonucleotides that yield long lived excited states increases with the oligomer's length [26, 28, 34]. The existence of excimer and exciplex states has also been recently supported by means of broadband time-resolved transient absorption spectroscopy in diribonucleosides containing adenine [35]. On the other hand, fluorescence up-conversion experiments performed by Markovitsi and co-workers both in synthetic [36, 37] and natural [38] DNA double-strand samples have been rationalised through the formation of an excitonic state delocalised over several nucleobases upon excitation, up to six according to some theoretical estimates [39],

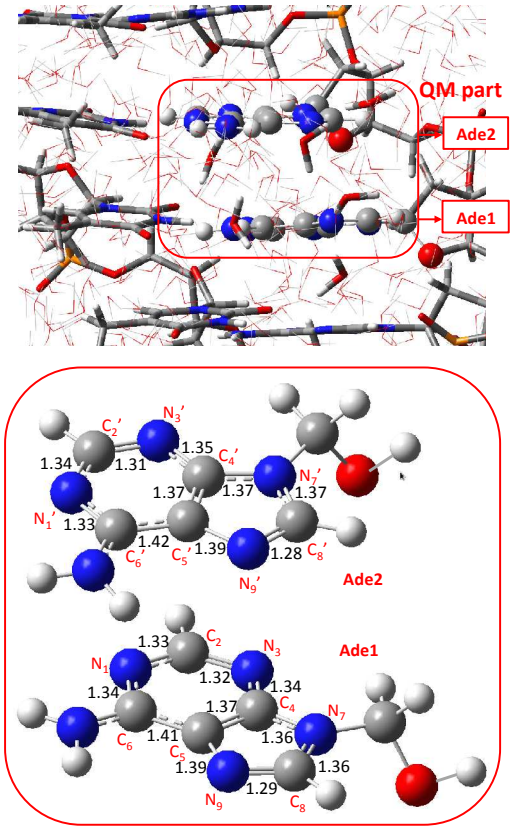

Figure 1 In the upper picture, red line highlights the QM couple of π-stacked adenines (Ade1 and Ade2, called *high* part, ball and stick representation) in the $d(A)_{10}$·$d(T)_{10}$ in water environment. The MM groups confining with the QM part (sugar-phosphate backbone, stacked and paired bases, H-bonded waters, called *medium* part, tube representation) are moving together with QM atoms during optimization calculations. The rest of the system (including bases, waters and counterions, *low* part, stick representation) were optimized after the former two parts converge. The lower picture shows enlarged QM parts, including bond length ground state minimum geometry (MinGS). Ade1 and Ade2 are the fourth and the fifth residues of the adenine strand.

thus conferring the long-lived component to the charge separation and charge recombination processes undergone along the relaxation of the delocalised excitation over several chromophores. More recent findings support the fact that long lived excited states decay more rapidly in A-T double stranded sequences than in single stranded $d(A)_n$ sequences[10], a feature also corroborated for the G-C base pairs and intrinsic of Watson-Crick (WC) base pairs hydrogen-bonding motifs[3, 11, 40-45]. The possibility that inter-strand proton transfer could play a role in the DNA deactivation mechanism is intriguing but will require further experimental and theoretical studies.

Many computational works have been recently undertaken on DNA multimers models, to elucidate how light interacts with this electronically and structurally complex system [27, 38, 46-54]. From a theoretical standpoint, Merchán and co-workers support the idea that the long-lived excited states seen in adenine homodimers originate from excimer state population, formed by two stacked bases. They show (at ab initio multireference CASPT2 level) that increasing the overlap of stacked adenines together with decreasing the distance between the two bases (in a perfect 'face-to-face' stacking), the energy of the CT excimer state decreases[48]. The flexibility is crucial for the formation and stabilization of excimers, with the totally overlapped conformation being almost not accessible in a constrained geometry like DNA, thus indicating that energetics and structures of the CT states strongly depends on the conformational properties of DNA. Recently, Lischka and co-workers[55], as well as Matsika and co-workers[56], computed the vertical absorption spectra of alternating adenine-thymine and $d(A)_{20}$-$d(T)_{20}$ oligomers using an hybrid quantum-mechanics/molecular-mechanics (QM/MM) scheme with two to four π-stacked adenines in the quantum region described with the algebraic diagrammatic construction method (ADC(2)). Both studies conclude that CT states contribute only to the high energy tail of the absorption spectrum. However, states of mixed local-CT character should be easily accessible at lower energies. In a recent paper, Rohlfing and co-workers [57] apply ab-initio many-body Green's function theory on small single-stand d(A)n and double-strand d(A-T)n multimers and argue that aqueous solvation may lower the energy of the CT states by more than 1 eV compared to wavefunction-based QM/MM. A QM/MM study by Lischka and co-workers[50, 54] employing *ab initio* multi-reference configuration interaction (MRCI) calculations on the adenine dinucleotide in water predicts the formation of several stable low lying exciplexes of nπ* and ππ* character with short inter-molecular separation (due to the high flexibility of the base), but without notable charge transfer. The authors argue that the longest lifetime results from trapping the system in these minima. Finally, employing TD-DFT calculations within a continuum (PCM) model, Barone and co-workers showed that a CT excimer is the absolute excited state minimum for water-solvated single- and double-stranded poly(A) multimers [49, 51, 58-60] and suggested that the long-lived component of the excited state population correspond to a dark excimer produced by inter-monomers charge transfer between stacked bases. However, a characterization of the CT deactivation pathway consistent with experimental data lifetimes remains indeterminate.

The present work encompasses a multireference ab initio (CASPT2//CASSCF) study in which the decay mechanisms of two stacked QM adenines are mapped within a realistic DNA environment $d(A)_{10}$·$d(T)_{10}$ described at the molecular mechanics level (see Figure 1). Thus properly modelling base-base *electronic interactions*, and how excitation energy can be shared and transferred between the two nucleobases to create new excited states such as excimer [1, 6, 10, 12, 13, 25, 26, 48, 49], exciton[38, 61-64] and/or CT states. [12, 13, 16, 17, 25, 27-29, 48, 50, 65]. At the same time, *steric hindrances* limiting the conformational freedom, which may affect the topology of the potential energy surface, as well as *electrostatic interactions* with stacked and paired bases, with the backbone groups, with the counterions and solvent (water) molecules are explicitly considered. This work goes far beyond our previous study of a single QM adenine within the same double strand environment (i.e., inter-base electronic interactions were fully neglected there).[66] Indeed, extension of the QM region to a second stacked adenine reveals an unprecedented mechanism for populating the CT state out of the initially excited bright (L_a) state: a common relaxation path appears for the two states that is based on the same leading geometrical deformation (C_2 puckering coordinate) and allow an energetically feasible internal conversion (IC) between the CT and L_a states.[67] However, direct decay from the CT to the ground state appears to be energetically too demanding and deactivation can only proceed though re-population of the original L_a state eventually following its natural deactivation path. Therefore, the proposed

mechanism reveals CT states as a natural traps and reservoirs of excited dimers, accounting for the longest lifetime component observed in time-resolved experiments.

Computational Details

(a) Ground State Classical Molecular Dynamics.

The starting geometry for the double-stranded $d(A)_{10}.d(T)_{10}$ DNA fragment was obtained following a classical 4 ns long molecular dynamics (using NTP at 300K, 1 bar and 2 fs timestep) starting from the crystallographic B'-DNA structure [68] (PDB ID code is 1PLY). AMBER-8 [69] program and ff03 force field [70] were applied. Explicit solvation by TIP3P water molecules with eighteen Na+ ions within a buffer of 10 Å and periodic boundary conditions were applied. The choice of the starting structure was done through a cluster analysis over the sampled snapshots, selecting the lowest energy optimized structure among the ten most stable structures of the largest cluster. The selected structure was further refined via QM/MM approach optimization (see following subsection). The scope was to produce a representative (average) structure of the investigated system. This structure was then employed for all the following QM/MM studies (see below).
Additionally, in order to obtain a larger sampling of DNA geometries for a more statistically accurate analysis of the available excitation energies for ππ* and CT states in the Franck Condon region, a ~150 ns MD simulation[71] was performed starting from the previously selected MM geometry. This study was aimed at producing a proper sampling of DNA geometries for a more statistically accurate analysis of the available excitation energies for ππ* and CT states in the Franck Condon region as intra- or inter-base parameters (for example stretching and stacked bases distances) changes in the ensemble. More details of the dynamics calculations are reported in the Electronic Supplementary Information section (ESI).

(b) QM/MM calculations: set up and active spaces

QM/MM calculations [72] were performed with the COBRAMM[73] interface developed by our group (presented in detail elsewhere [73]). The adopted selection for the QM region (shown in the bottom part of Figure 1) produces a charge distribution on the nucleobase and its □-system that reflects the covalent link between the adenine and the sugar ring. This makes the choice suitable for this kind of investigation. It includes both the sugar ring carbon directly linked to the base and the adjacent oxygen atom; a hydrogen link-atom approach has been adopted. A three layers (*high*, *medium* and *low*) approach was used: the fourth and fifth π-stacked adenines (called Ade(1) and Ade(2) respectively, numbering from the 5-position of the poly(dA).poly(dT) decamer) were included in the QM region (*high* layer, inside the red line in Fig. 1) and were described at SA-CASSCF level, while all the rest was described classically. The MM groups adjacent to the QM region (sugar-phosphate backbone, stacked and paired bases, H-bonded waters) were included in the movable *medium* layer (the part out of the red line in Figure 1). The remaining MM atoms (six couples of bases plus the corresponding backbone and bulk waters), i.e. the *low* layer, were optimized, in each step, after the *high*+*medium* parts converged (see ref. 73). Both the Gaussian-03 [74] and AMBER-8 packages were employed during QM/MM computations [75]. CASSCF/AMBER energies were refined at CASPT2 level to account for correlation effects.

INTER-BASE STUCTURAL PARAMETERS

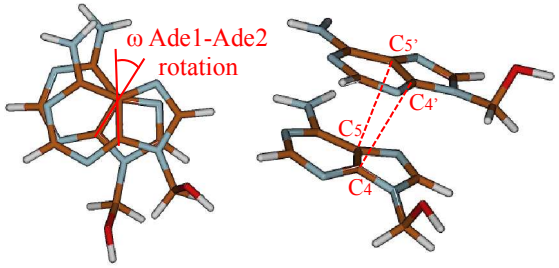

	ω	C4-C4'	C5-C5'
MinGS	35°	4.67	4.20
$MinCT_{12}$	26°	4.16	3.55
$MinCT_{21}$	31°	4.22	3.67
Dyn1	31°	3.25	3.14
Dyn2	28°	3.20	3.19
Dyn3	33°	3.14	3.27

Scheme 1

[76, 77] MOLCAS-7.7 [78] was used for the CASPT2 computation by modelling the environment with AMBER point charges [75]. The QM/MM optimizations were done at CASSCF(8,8)/6-31g* level, thereby including four π and four π* orbitals in the active space. In particular, the active space encompasses the HOMO-1, the HOMO, the LUMO and the LUMO+1 orbitals on each base. In this way we could compute simultaneously L_a, L_b, CT, B_a and B_b states. On top of each CASSCF optimized geometry three different SA-CASSCF//CASPT2/6-31g* single point computations were performed: (a) SA-5-CAS(8,8) averaging over five states to evaluate ππ* energy profiles along $L_a(1)$ and $L_a(2)$ decay routes; (b) SA-7-CAS(12,10) by adding the two n orbitals, localized on the two adenines, aimed at resolving the positions of the nπ* states along the L_a decay paths; (c) SA-12-CAS(8,8) thereby resolving the energetics of the two lowest charge transfer states, involving an electron transition from Ade1 to Ade2 (CT_{12}) and the other way round (CT_{21}). Conical Intersection (CI) geometries were found with the conical intersection optimizer developed within the COBRAMM code (see section S9 in ESI).

(c) Reaction path calculation strategy

Several previous works [5, 66, 67, 79-91] identify C_2 ring puckering (here defined by the dihedral angle $\theta = C_2N_1C_4C_5$), followed by hydrogen out-of-plane modes (defined by the dihedral angle □ $= H_2N_1C_4C_5$), as the adenine distortion coordinate leading to the L_a/S_0 CI and the ultrafast decay of the nucleobase monomers along L_a (Figure 2). Thus, the photoinduced motion computed along adenine L_a deactivation path [66, 67] provides the basis for the optimized scan employed here to map the adenine decay routes on both the L_a surfaces, from the Franck Condon (FC) region to the L_a/S_0 CI. In the present work, L_a MEPs are computed by optimized scans at fixed increasing values of the $C_6N_1C_2N_3$ and $C'_6N'_1C'_2N'_3$ dihedral distortion values respectively, that (jointly to the $N_1C_2N_3C_4$ and $N'_1C'_2N'_3C'_4$

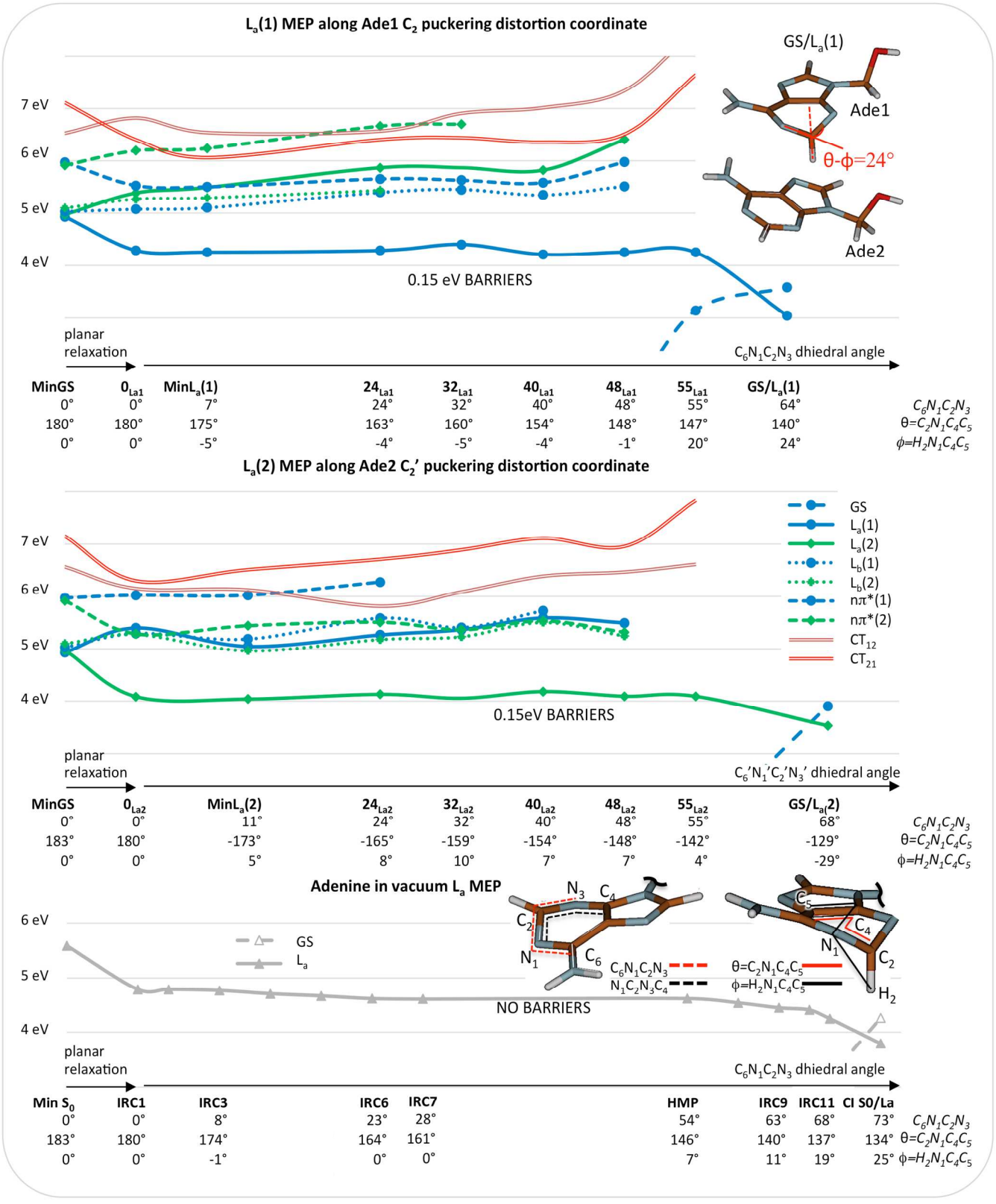

Figure 2 CASPT2//CASSCF(8,8)/6-31g*-SA5 energy profiles along the relaxation path computed along the $L_a(1)$ state and $L_a(2)$ state in the MM DNA d(A)10.d(T)10 environment (first and second windows, respectively). SA-12 CT_{21} and CT_{12} energies are included in the pictures. L_b and nπ* CASSCF(12,11) states are calculated at SA7-CASPT2//CASSCF(12,10) level. Energy values are in Table 1 and are shifted on the MinGS lowest excited state value of SA5 calculation. The third graph represents CASPT2//CASSCF(12,11)/6-31+g**-SA-9 potential energy surface profiles along L_a minimum energy path (MEP) of adenine in vacuum. Full and empty triangles correspond to CASPT2 and multistate-CASPT2, respectively (see ref [67]). θ and □ represent the out of purine plane bending angle of C_2 and H_2, respectively.

Table 1. SA-5 CASPT2//CASSCF (8,8)/6-31g*/AMBER relative energies (ΔE,eV) for the relevant points along the $L_a(1)$ (upper table) and $L_a(2)$ (lower table) decay paths ($C_6N_1C_2N_3$ dihedral angle rotation) of two QM adenines (Ade1 and Ade2, Figure1). See 'Reaction path calculation strategy' section for more information. The active space consists of four π (HOMO and HOMO-1 orbital for each base) and four π* orbitals (LUMO and LUMO+1 for each base).[a] SA-7-CASSCF(12,10)//CASPT2/6-31g*/AMBER relative energies (ΔE,eV). The active space consists of four π two n orbitals localized on each base and four π* orbitals. [b] SA-12 CASPT2//CASSCF (8,8)/6-31g*/AMBER relative energies (ΔE,eV). CASSCF includes four π and four π* orbitals. Extended tables for each state average calculation are reprted in section S7 of ESI.

	MinGS 0°	**0_{La1}** 0°	**MinL_a(1)** 7°	**24_{La1}** 24°	**32_{La1}** 32°	**40_{La1}** 40°	**48_{La1}** 48°	**55_{La1}** 55°	**L_a(1)/GS CI** 64°
GS	0.00	0.26	0.30	0.69	0.82	0.95	1.45	3.14	3.58
L_a(1)	4.93	4.28	4.25	4.28	4.40	4.21	4.25	4.25	3.04
L_a(2)	4.97	5.39	5.49	5.87	5.87	5.82	6.40		
L_b(1) [a]	5.10	5.15	5.17	5.47	5.52	5.42	5.58		
L_b(2) [a]	5.17	5.34	5.36	5.51					
nπ*(1) [a]	6.04	5.60	5.57	5.73	5.70	5.65	6.05		
nπ*(2) [a]	5.98	6.26	6.31	6.73	6.77				
CT_{12} [b]	6.40	6.64	6.41	6.44	6.78	6.89	7.21	8.38	
CT_{21} [b]	6.99	6.06	5.93	6.27	6.31	6.22	6.38	7.51	
	MinGS 0°	**0_{La2}** 0°	**MinL_a(2)** 11°	**24_{La2}** 24°	**32_{La2}** 32°	**40_{La2}** 40°	**48_{La2}** 48°	**55_{La2}** 55°	**L_a(2)/GS CI** 68°
GS	0.00	0.11	0.13	0.35	0.49	0.80	0.99	1.55	3.90
L_a(1)	4.93	5.40	5.05	5.27	5.37	5.59	5.50		
La(2)	4.97	4.08	4.04	4.13	4.05	4.18	4.09	4.09	3.53
Lb(1) [a]	5.10	5.36	5.26	5.65	5.48	5.79			
Lb(2) [a]	5.17	5.35	5.03	5.25	5.30	5.57	5.32		
nπ*(1) [a]	6.04		6.09	6.34					
nπ*(2) [a]	5.98	5.36	5.51	5.58	5.43	5.60	5.39		
CT_{12} [b]	6.40	5.98	5.95	5.64	5.91	6.22	6.30	6.44	
CT_{21} [b]	6.99	6.13	6.34	6.54	6.72	6.95	6.79	7.66	

twisting) governs the C_2 and C_2' ring puckerings of $L_a(1)$ and $L_a(2)$ (localized on Ade1 and Ade2 respectively).
The simultaneous dihedral rotation of both dihedral angles creates the C_2 out of plane motion, evaluated as θ, called ring puckering (Figure 2). Additionally, CT_{12}, CT_{21} MEPs were also evaluated along the same reaction coordinate ($C_6N_1C_2N_3$ and $C'_6N'_1C'_2N'_3$ dihedral distortion, respectively).

Results and Discussion

(a) Ground State Geometry analysis

Ground state optimized geometry (MinGS) at QM/MM level of the two stacked QM adenines shown in Figure 1 essentially reproduces/matches the planar structure previously calculated for a single QM Adenine, both in DNA environment and in vacuum (see Scheme S1 in ESI)[66, 67].
The stacked bases conformation can be defined by three descriptors (see Scheme 1), the two inter-base distances C_4-C_4' and C_5-C_5', and the twisting angle ω=$C_4C_5C_5'C_4'$. In the optimized QM/MM structure, the inter-base distance and twisting angle values are 3.69 Å and 35°, respectively, in satisfactory agreement with analysis of X-ray diffraction data from a polycrystalline and well oriented fiber of the sodium salt of poly(dA).poly(dT)[68].

(b) Vertical excitation energies

Computed vertical excitation energies show that bright L_a states (La(1) and La(2) localized on Ade1 and Ade2, respectively, see Fig. 1) are the lowest excited states (4.93 and 4.97 eV, respectively), with the L_b states only ~0.10 eV above (see Table 1). Moreover, we observe that the lowest-energy absorption band is caused by exciton states delocalized over the two bases. This is originated by the linear combination of the two ππ* absorbing HOMO→LUMO transitions (L_a configurations) of the different monomers. The shared excitation between the two bases is confirmed at different level of calculations, including SA calculations with five, seven and twelve electronic states (see Table S1 in ESI).
Interestingly, the nπ* states, which in gas-phase lie below the L_a band, are blue-shifted in the solvated $d(A)_{10}.d(T)_{10}$ environment up to 6 eV, becoming energetically inaccessible [1, 92-95]CT states are considerably higher than L_a absorption energies: CT_{12} and CT_{21} are at 6.40 eV and 6.99 eV respectively in the Franck Condon region (see Table 1). The agreement of the calculated L_a absorption energies with the experimental absorption band energies (4.79 eV recordered in a poly-d(A)n·d(T)n duplex[61]) is encouraging and validates the computational procedure and QM/MM model employed. [1, 9, 96-98]

(c) (L_a) states deactivation of two stacked adenines in $d(A)_{10}$ ·$d(T)_{10}$ DNA multimer

The calculated MEP profiles along the puckering $L_a(1)$ and $L_a(2)$ relaxation coordinates ($C_6N_1C_2N_3$ and $C'_6N'_1C'_2N'_3$ respectively, details in Computational Details section) are given in Figure 2, while energy values are reported in Table 1. Different levels of calculations were necessary to include all the relevant states in the excited adenine deactivation path (see Computational Details section).

Table 2 SA-5-CASSCF(8,8)//CASPT2/6-31g*/AMBER S_N-GS energy gaps (eV) and relative oscillator strength (in parenthesis) obtained from SA-5-CASSCF(8,8)//CASPT2/6-31G*/AMBER (L_a) and SA-12-CASSCF(8,8)//CASPT2/6-31G*/AMBER (CT) calculations. The active space consists of four π and four π* orbitals.

	MinGS 0°	**0_{La1}** 0°	**MinL_a(1)** 7°	**24_{La1}** 24°	**32_{La1}** 32°	**40_{La1}** 40°	**48_{La1}** 48°	**55_{La1}** 55°	
La(1)-GS	4.93(0.61)	4.02(0.15)	3.95(0.15)	3.59(0.14)	3.58(0.11)	3.26(0.11)	2.8(0.10)	1.11(0.05)	
	MinGS 0°	0_{La2} 0°	MinL_a(2) 11°	13_{La2} 13°	24_{La2} 24°	32_{La2} 32°	40_{La2} 40°	48_{La2} 48°	55_{La2} 55°
La(2)-GS	4.97(0.06)	3.97(0.13)	3.91(0.11)	3.88(0.14)	3.78(0.11)	3.56(0.11)	3.38(0.11)	3.1(0.10)	2.54(0.09)
	0_{CT21} 0°	MinCT_{21} 7°	24_{CT21} 24°	32_{CT21} 32°					
CT_{21}-GS	3.73(0.01)	3.65(0.01)	3.58(0.01)	3.55(0.01)					

Very notably, the L_a deactivation paths computed here for each base, reasonably match the MEP previously computed for a single QM adenine in vacuum[67] (see the bottom of Figure 2) and in the double stand, validating the previous study for localized excitations[66]. However, since two QM adenines are included in the current model, CT states can be plotted together with localized states to understand the role that they play in the deactivation path.

We compare the L_a(1) and the L_a(2) deactivation paths of the stacked adenines (Ade1 and Ade2, respectively) in the DNA-like environment (upper and middle panels in Figure 2) with the L_a path of adenine monomer in vacuum (lower panel in Figure 2)[67]. Bond planar relaxation of the bases drive the system out the Franck-Condon region, lowering the energy by ~1.00 eV. Afterwards the system follows C_2 puckering distortion (θ values given in Figure 2) on either monomer. The wavefunction analysis shows that an intra-monomer character substitutes the exciton nature already during the initial planar relaxation on the L_a energy surface, explaining why the distortion localizes on a single base. The L_a energy profiles along the puckering coordinate are remarkably flat, (even more than adenine in vacuum), see Table 1 and Figure 2: the L_a states energies remain substantially unchanged from the planar relaxed structure (0°) until ~ 55° rotation, indicating absence of a clear well-directed gradient. Moreover, both paths show small barriers (~0.15 eV), that are absent in vacuum, induced by electronic and steric influence. Despite locating minima (computed without any constraints) at the CASSCF level (hereafter denoted as MinL_a(1) and MinL_a(2)) has been possible, the CASPT2 correction clearly demonstrates that the Potential Energy Surface (PES) remains very flat making it hard to define a real L_a minima. The surface profile decreases significantly only beyond ~ 55° distortion.

The calculated L_a profiles justifies the two different decay time ranges observed in the DNA multimer systems[10-16]: (a) the monomer-like lifetimes (τ_1 and τ_2, in the order of hundreds of fs to a few ps), plus (b) the longer lifetime component (τ_3, in the order of tens to hundreds ps).

(a) The similar shapes found for L_a in vacuum and in DNA, suggests that the two fastest decays observed for isolated[67] and for stacked adenines (τ_1=0.39 and τ_2=4.3 ps) [6] involve an intra-molecular process and follow the same fate documented for isolated adenine. They can be assigned to the initial relaxation and ring puckering distortion on the C_2 atom (τ_1), followed by the activation of the hydrogen out-of-plane bending (τ_2), which opens the decay process on ground state. We assume that the system does not completely relax in the plateau region. This means that the excess of vibrational energy allows accessing the L_a/GS crossing virtually without overpassing any barrier. In this case (like in vacuum) the L_a plateau acts as a dynamical barrier that only slows the decay toward the L_a/GS crossing and gives origin to the biexponential decay kinetics (τ_1+τ_2).

(b) At the same time, the L_a profiles of the dimer are compatible with the slowest decay time, τ_3 (in the order of hundred ps) as already pointed out in our previous study: it could be assigned to the slower process needed to overcome the environment-generated barriers (steric, electrostatic and electronic effect). Interestingly, simple kinetic considerations show that a room temperature process with a lifetime of 100 ps corresponds to a barrier of 0.16 eV, in good agreement with the computed barriers (see ESI). The height of the L_a barriers slightly fluctuates depending on the parameters of the computations (compare Table 1 with Table S2 and Table S4 in ESI, where just active space and state average parameters are changing). This outcome strongly suggests that a barrier, related to the L_a relaxation, always exist in the DNA environment, enlarging the excited state lifetime. The latter path provide a route for a full dissipation of the vibrational energy in the environment during the relaxation on the L_a plateau, requiring hundreds of ps to overpass the barrier (τ_1+τ_2+τ_3). While we consider that our results are only qualitative, they give a satisfactory indication of the influence of the DNA environment on the deformation motion of the adenine ring. The fluorescence associated with the longest lifetime (~3.2 eV) measured for $d(A)_{20}$ in water[6] are also in qualitative agreement with the L_a-GS energy gaps in the L_a states plateau region (from 3.95 to 2.8 eV values) evaluated in our calculations (see L_a-GS energy gaps from both MinL_a(1) and MinL_a(2) to 48° dihedral distortion in Table 2). The calculated L_a profile findings contradicts the large part of the literature which addresses the slowest decay of multimers to a process involving an excimer or exciplex formation. However, in the section below we show that these different scenarios can actually coexist.

(d) CT states population and deactivation paths

Along the L_a de-excitation pathways the lowest CT states, CT_{12} and CT_{21}, lie too high in energy to interact with L_a states (Figure 2, upper and middle panels). In the following, we shall investigate the possibility of structural deformations that will bring the CT and the L_a states closer, or even allow a crossing, thus making feasible population of CT states either out of the L_a state via vibrational energy redistribution and internal conversion, or directly upon GS excitations. To study the former mechanism we (i) characterize the CT minima structures and energies, (ii) perform constrained optimizations of the CT states along the $C_6N_1C_2N_3$ distortion coordinate driving the L_a decay, (iii) map the topology of the PES connecting L_a and CT profiles, extracting geometries required for an $L_a \rightarrow$CT IC, (iv) characterize the decay paths out of the CT minima leading to conical intersections with the GS or L_a states; and (*v*) perform a long GS molecular dynamics simulation to investigate the possibility of populating CT states upon direct vertical excitation. The latter step allows to elucidate the correlation between CT energetics and DNA sampled conformations through excited state calculations at selected snapshots, fulfilling a set of criteria for the expected stabilization of the CT states.

MinGS vs MinCT: Ade1-Ade2 reducing distance

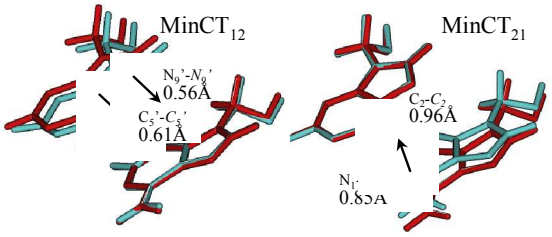

Scheme 2

(i) Upon geometry optimization, the CT_{12} and the CT_{21} states are stabilized down to the first excited state, i.e. below the L_a band (see Figure 3). The CT_{12} and CT_{21} minima ($MinCT_{12}$ and $MinCT_{21}$, respectively) are shown in Scheme 2 (blue colour) where the main structural differences with respect to the ground state equilibrium geometry MinGS (red colour) are highlighted. The most evident changes are the decreasing of the distances between C_4-C_4' and C_5-C_5', as well as of the base-base twisting angle□□, allowing for a better alignment and, thus, increased orbital overlap. These three coordinates lower the excimer state energy, as documented earlier[48]. With values of 14° and 7° at $MinCT_{12}$ and $MinCT_{21}$ for the $C_6'N_1'C_2'N_3'$ and $C_6N_1C_2N_3$ angle respectively, *the C_2 puckering distortion emerges as a common feature of both the L_a and CT relaxation pathways*. Along the L_a deactivation pathway the puckering is a result of the CN-methanamine-like twist around the C_2-N_3 double bond, necessary to reach the CI (Figure 4). Along the CT_{21} ($CT1_2$) deactivation pathway the puckering is a consequence of the high electron density in the Ade1 (Ade2) □-system and the consequential increase of partial negative charge on C_2 (C_2') and N_3 (N_3') (atoms charge distribution is provided in the ESI). The puckering leads to a tetrahedral conformation (pyramidalization) of the atoms, allowing to better shield the excess negative charge (Figure 4). The different causes that induce the puckering distortion influence in different ways the intra-base bond lengths changes in MinLa and in MinCT structures. Specifically, the C_2-N_3 torsion requires a larger bond

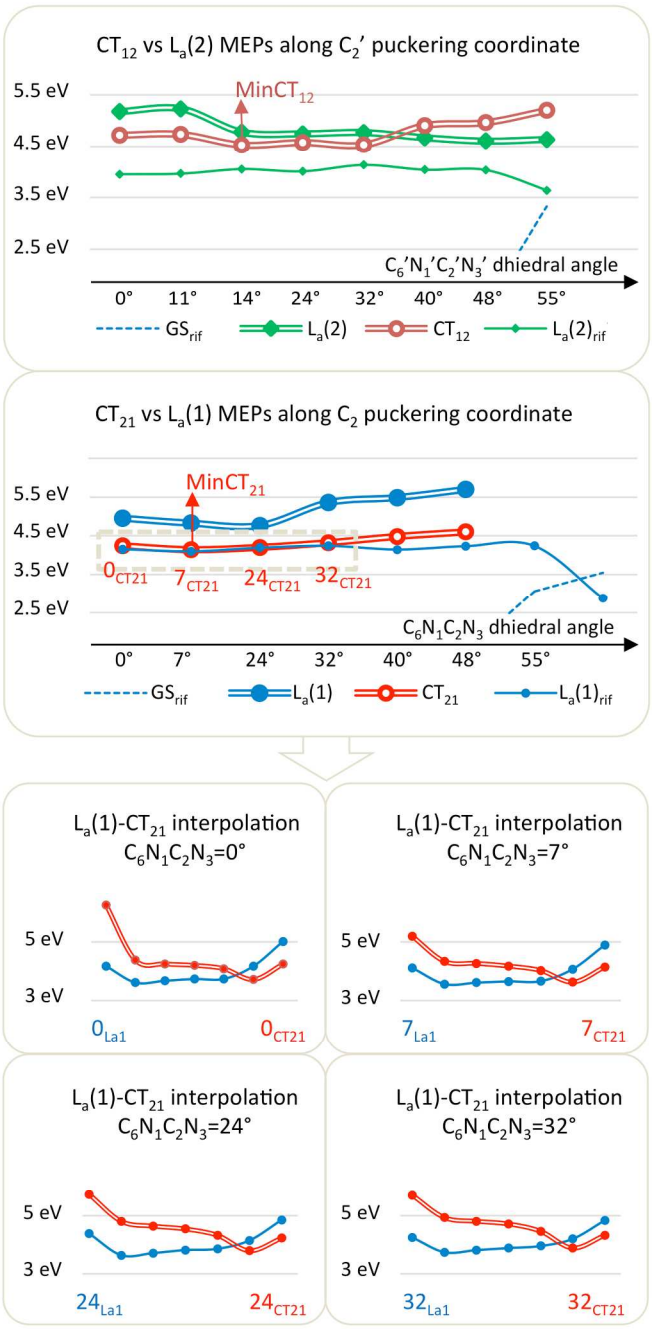

Figure 3. First and second panels represent the CASPT2//CASSCF(8,8)/6-31g*-SA12 CT_{12} and CT_{21} MEP along the $C_6N_1C_2N_3$ and $C_6'N_1'C_2'N_3'$ distortion coordinate on Ade2 an Ade1 respectively (Table S5 in ESI section), starting from the planar (0°) optimized geometry. The thin lines are the $L_a(1)$ and $L_a(2)$ minimum energy path along the same coordinate ($La(1)_{rif}$ and $La(2)_{rif}$, respectively, values in Table S4). Third panel shows the CASPT2//CASSCF(8,8)/6-31g*-SA8 interpolation between the optimized $L_a(1)$ (0_{La}, 7_{La}, 24_{La} and 32_{La}) and the optimized CT_{21} (0_{CT21}, 7_{CT21}, 24_{CT21} and 32_{CT21}) at 0°, 7°, 24°, 32° $C_6N_1C_2N_3$ dihedral distortion on Ade1 (energy values in Table S6).

stretching comparing with a C_2 pyramidalization distortion. We suppose that the higher stabilization of CT_{21} comparing with CT_{12} minimum (see Table S5) is a consequence of the base stacked inter-base orientation (in particular base-base rotation).

The distortion on Ade1 reduces the C_2-C_4' distance, that stabilize the CT_{21} charge redistribution. In the CT12 case, the puckering does not lead C_2' distortion to approach a positive charged part of Ade1, because of the base-base rotation angle between stacked bases, and charge stabilization is hindered. Technical details on charge redistribution and CT minima structures are in the ESI section.

(ii) The MEPs of CT_{12} and CT_{21} along the common $C_6N_1C_2N_3$ distortion coordinate are shown in Figure 3. The first panel shows that CT_{12} state is more or less isoenergetic with the $L_a(2)$ state along the dihedral distortion axis, but they are both higher than the $L_a(2)$ MEP energy profile (thin line). The energy gap between Min$L_a(2)$ and MinCT_{12} (energy values in Table S5 and S4 in ESI) is ~0.7 eV. So, it is reasonable to assume that is very unlikely to access the CT_{12} surface from $L_a(2)$ decay path. The second panel shows that the optimized CT_{21} profile is lower than the $L_a(1)$. At the same time we can see that the CT_{21} profile is isoenergetic with the $L_a(1)$ MEP (thin line) from 0° to 32° puckering values. This opens the possibility to access to the CT_{21} state.

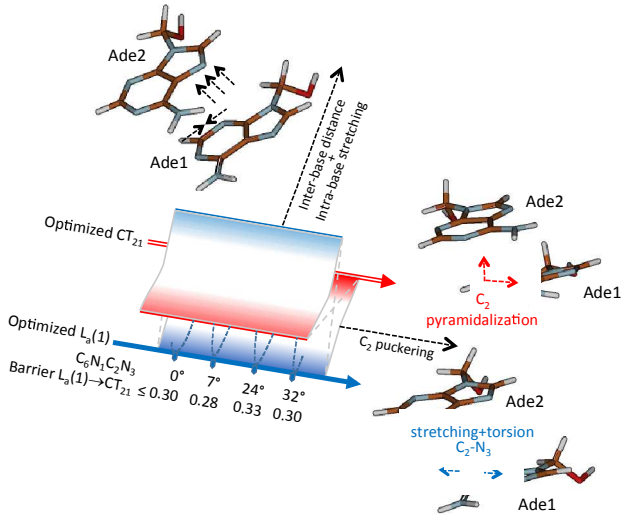

Figura 4. Cartoon like representation of the population transfer between $L_a(1)$ and CT_{21} states along the inter-base distance plus intra-base stretching coordinate, orthogonal to puckering distortion coordinate. C_2 puckering is the $L_a(1)$ and CT_{21} common relaxation coordinate: in the $L_a(1)$ state originates from a C_2-N_3 stretching followed by torsion (blue dashed rows), in the CT_{21} state it originates from the C_2 pyramidalization distortion (red dashed rows).

(iii) To evaluate the opportunity to populate CT_{21} from $L_a(1)$, we map the topology of the S_1 potential energy surface between $L_a(1)$ and CT_{21} we have performed interpolations between $L_a(1)$ and CT_{21} geometries, optimized at the same dihedral angle values. The graphs for four puckering angles (0°, 7°, 24° and 32°) are shown at the bottom of Figure 3, following the orthogonal intra-base stretching coordinate. Upon increasing the distortion (over 32°) the barriers become higher (see Table S6). The $L_a(1)\leftrightarrow CT_{21}$ exchange involves mainly intra-monomer stretching of bonds C_2-N_3 and C_4-C_5, as well as shortening of the inter-base distance (values in Figure S1 in SI), as shown in cartoon-like picture in Figure 4. The increase of C_2-N_3 L_a bond length matches with the ethylene-like excited state that leads to rotation on this bond, explained above in (i). The interpolations show that the $L_a(1)$ and the CT_{21} minima values at the fixed dihedral angle are a bit shifted (toward CT_{21} and $L_a(1)$ respectively) at the CASPT2 level as compared to CASSCF calculations, making more feasible the population transfer. In Figure 4 we show the barriers, that have been estimated a the crossing point between the CT_{21} and $L_a(1)$ (values are also reported in Table S6). The path on S_1 that is leading from a CT_{21} to a $L_a(1)$ excited state is likely to involve an avoided crossing transition state instead of a real crossing, as indicated by our calculations that were never able to identify S_2/S_1 real crossing points.. It is apparent that the documented barriers provide an upper limit for the real activation energies (≤0.28 eV), falling therefore in the same range as the intra-monomer barriers calculated along the $L_a(1)$ and $L_a(2)$ deactivation paths[99]. Therefore, because of these relatively small energy barriers and the little structural differences between CT_{21} and $L_a(1)$ geometries, $L_a(1)\leftrightarrow CT_{21}$ population transfer is likely to compete with the L_a deactivation route. Moreover the CT_{21}-GS energy gaps along the CT_{21} MEP (~3.6 eV, Table 2) match reasonably well with the fluorescence experimental data at the longest lifetime, τ_3 (3.2 eV) [6], not far from the L_a-GS energy gaps calculated along the L_a plateau and discussed above. This could address excited state population during the τ_3 lifetime to both L_a and CT_{21} states.

(iv) After unravelling the possible scenario for populating the CT_{21} state from $L_a(1)$ decay pathway, we characterize feasible deactivation paths out of the CT_{21} minimum by looking at conical intersections between this state and the GS (see right part of Scheme 3 and Table S5). Two different CIs were found out of the CT_{21} minimum: the lowest energy CI (CI CT_{21}/GS PT) is characterized by a proton transfer between the amino groups, where the protons hops from Ade2 to Ade1 (lower-right part of Scheme 3), neutralizing the charges; this CI is located 0.48 eV lower then MinCT_{21}. However, the optimized path to reach this CI shows a 0.9 eV activation barrier (see Figure 5). A second CI between the CT_{21} minimum and the GS was characterized (CI CT_{21}/GS) which involves shortening of the inter-base distance (see upper-right part of Scheme 3), together with N_{am} and C_2 pyramidalization, that shift the excess electron density toward the positively charged Ade2 and thus facilitating charges neutralization; this CI is 1.1 eV above MinCT_{21} geometry. Besides the severe out-of-plane deformation observed in this second CI, which breaks the aromaticity of the nucleobases, an important effect is the distruption of the H-bond pattern involving the thymine WC paired base of Ade1 towards the CI (shown in Figure S2 in ESI section). While this

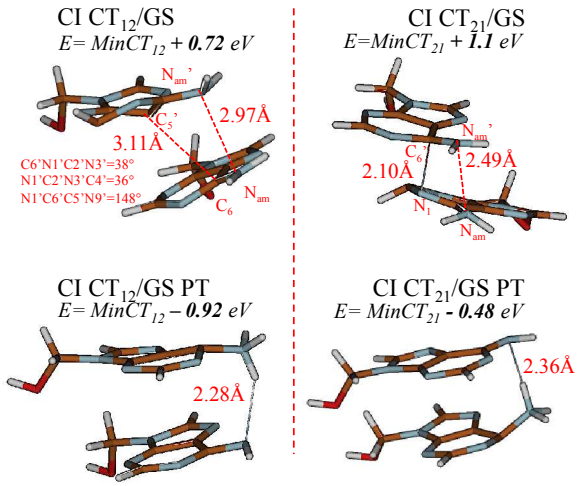

Scheme 3

effect is not fully accounted within the QM/MM scheme employed here, we expect that a wavefunction description of the paired thymine bases would probably forbid large out of plane deformations, as required to reach CI-CT_{21}/GS, further increasing the energies of the CIs. The corresponding CIs with the GS found for the other CT state (CT_{12}) (CI CT_{12}/GS PT and CI CT_{12}/GS, Scheme 3) behave similarly.

The size of the barriers to reach those CT/GS CIs indicates that the more plausible way to decay to the GS is to return back to $L_a(1)$ and then follow the usual $L_a(1)$ deactivation path. The barriers associated with this kind of mechanism suggest lifetimes comparable with the longest lifetime (τ_3) observed experimentally in these systems, a scenario further supported by the estimated fluorescence energies that match (within the computational errors) the observed ones.

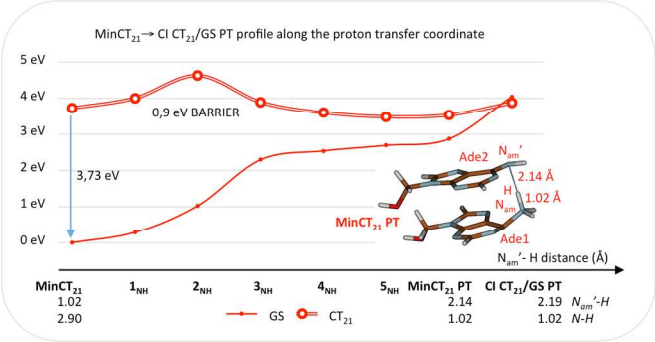

Figure 5. CASPT2//CASSCF(14,12)/6-31+g**-SA2 optimized scan between $MinCT_{21}$ and CI CT_{21}/GS PT ($MinCT_{21}$ PT) along N_{am}'-H distance coordinate. Energy values in Table S7 in ESI section.

(v) Finally, we explore the possibility to populate the CT states directly upon excitation, a hypothesis that is ruled out when considering the electronic structure of the QM/MM GS optimized geometry at the FC region, where CT states are very high in energy (6 eV above the GS). To this aim, we run a 150 ns MD dynamics of $d(A)_{10}{\cdot}d(T)_{10}$ double strand in water at room temperature, sampling a relatively large number of ground state conformations. In particular, we are looking for structures where the two adenines are closer and overlap more efficiently, thus lowering the excimer states energie[48] . Three structures were selected with the smallest average values for the C_4-C_4' and C_5-C_5' distances and we calculated their vertical energies and oscillator strengths at the MM geometries. Inter-base geometry parameters are shown in table of Scheme 1 with the acronyms Dyn1, Dyn2 and Dyn3, respectively (see also SI). Even if the inter-base distances and the twist angle values are even lower than what we find at the CT minima (see Scheme 1 parameters), the lowest CT state is still at least 0.8 eV above the L_a bands. This indicates that the inter-base distance alone is not responsible for stabilizing CT states. The CT energy is also very sensitive to the intra-base bond lengths, which delocalize the charges. This implies that the stabilization of the CT is a dynamical process, connected with both inter- and intra-molecular vibrations, as shown in Figure 4, and that a more elaborate and extensive analysis of sampled configurations must be performed. The analysis of the GS relaxed geometries, performed in this and other studies, may thus overestimate the positions of the CT states. Additionally, Dyn1, Dyn2 and Dyn3 show low energy states possessing exciton and CT mixing character. These results suggest (a) that electronic configuration mixing plays an important role in the photophysics of oligo nucleotides and (b) that the conformational flexibility of oligonucleotides may play a basic role for their photophysical properties. These results are confirmed by the absorption and CD spectra of a wide ensemble of ground state configuration (~200) obtained through QM/MM simulation of $(dA)_{20}(dT)_{20}$ oligonucleotide[56], and the possibility to directly populate the CT state from the FC region cannot be completely ruled out. The position and the population of the CT states in the Franck Condon region is still an hot topic[56, 57] that requires further computational investigations. More information about wave functions and energies of Dyn1, Dyn2 and Dyn3 geometries are shown in the SI section (Table S8).

(e) Role of L_b and nπ* states

The different timescale of excited state dynamics observed in single gas-phase monomers and solvated multimer calls for a critical assessment of the computational results and the mechanistic scheme drawn out of these data. In particular, our results speak for a possible population transfer between L_a and CT states in the dimer that is otherwise inaccessible during the ultrafast deactivation of the isolated monomer. On the other hand, speculations that the L_b and nπ* states are not populated due to weak vibronic couplings, as suggested by the rotational analysis of the vibrational bands in resonance enhanced two-photon ionization (R2PI) spectra [100] of the monomer, may not hold here, since even a weak coupling could lead to appreciable population transfer over the 100 ps timescale of the longer decay component. Therefore, the proposed internal conversion mechanism involving L_a↔CT transfer can be generalized to any low lying state sharing common relaxation deformations with the L_a state (as it happens indeed in CT states). Gas-phase studies document a planar minimum for the L_b state [67, 101], lacking the characteristic C_2 puckering with stretching modes different from the ones observed along the L_a MEP. Consequently, L_b relaxation from Franck Condon region occurs in an orthogonal direction compared to the relaxation of the bright L_a state, letting us conclude that the L_a↔L_b internal conversion process is still inefficient. Concerning nπ* states, however, theoretical studies in vacuo document that the relaxation leading to nπ* minimum involves also a C_2 puckering distortion [67, 101]. This is not surprising as n→π* excitation leads to an increase of the π-electron density, similarly to the net effect of a CT transition. Therefore, we suggest that internal conversion to the nπ* state may also be a feasible trapping mechanism in adenine multimers, allowing for a population transfer from the L_a channel. In support of this hypothesis our calculations demonstrate that the nπ* state exhibit a pronounced stabilization of ~0.5 eV along the excited state profiles of the L_a states (see Table 1, stabilization of nπ*(1) along the MEP on $L_a(1)$ and stabilization of nπ*(2) along the MEP of $L_a(2)$), a behaviour similar to that seen for CT states. The role of nπ* states in the deactivation process in adenine multimers will be analysed in a forthcoming work.

Conclusions

Extending the QM region to two-stacked adenines in QM/MM calculations of a double-strand DNA $(dA)_{10}$-$(dT)_{10}$ multimer reveals that C_2 puckering is a relaxation coordinate common to both L_a and CT states. We show that population transfer between these states is energetically feasible and is likely to occur via vibrational energy redistribution into orthogonal modes that connect L_a and CT states. Our results suggest that

the longest lifetime component observed in $d(A)_n$-$d(T)_n$ oligomers (in the order of hundred ps) may be due to both a) a direct intra-monomer mechanism involving relaxation on the localized $L_a(1)$ and $L_a(2)$ states and their decay along a (small) barrier controlled path leading to a CI with the ground state, and b) a population transfer to a CT state that would thus act as a trap and reservoir of excited dimers. In this latter case, we clearly show that direct decay of the CT state to the GS via a conical intersection is too demanding energetically, and back-transfer and population to the original L_a state needs to occur for triggering decay to the ground state (by following the usual intra-monomer decay route).

Dynamical simulations joint to ultra-resolved transient spectroscopies may possibly reveal the oscillations between L_a and CT states responsible for this transfer/back-transfer process, also showing if population transfer is a coherent process or instead involves population splitting and spreading on the PES. In the future, we plan to extend the QM region to the two WC paired thymines in order to investigate the inter-strand interactions that could also play a role in the deactivation process, as some experiments and computations suggest[10]. For instance, direct proton transfer between Adenine-Thymine WC base pairs could possibly trigger an alternative and more efficient mechanism for deactivation of the CT states (e.g., the barrier that leads to the proton transfer CI with the GS could be lowered, if the proton involved is transferred to the H-bonded oxygen of the paired Thymine instead of the stacked Adenine), thus enlightening the full reaction pattern accessible by the system.

Acknowledgements

M.G. acknowledges support by the European Research Council Advanced Grant STRATUS (ERC-2011-AdG No. 291198).

Notes and references

[a] Dipartimento di Chimica "G. Ciamician", Università di Bologna, via F. Selmi 2, Bologna, 40126, Italy
[b] Zentraler Informatikdienst, Technische Universität Wien, Wiedner Hauptstraße 8-10 / 020, 1040 Wien
[c] Department of Physics, Michigan Technological University, 1400 Townsend Drive, Houghton, MI, 49331-1295, USA
[d] Université de Lyon, CNRS, Institut de Chimie de Lyon, École Normale Supérieure de Lyon, 46 Allée d'Italie, F-69364 Lyon Cedex 07, France
[e] Laboratoire de Chimie, Ecole Normale Supérieure de Lyon, 46 allée d'Italie, 69364, Lyon, France.

Electronic Supplementary Information (ESI) available: [details of any supplementary information available should be included here]. See DOI: 10.1039/b000000x/

1. C. E. Crespo-Hernandez, B. Cohen, P. M. Hare and B. Kohler, *Chem. Rev.*, 2004, 104, 1977-2020.
2. C. T. Middleton, K. de La Harpe, C. Su, Y. K. Law, C. E. Crespo-HernÃ¡ndez and B. Kohler, *Annu. Rev. Phys. Chem.*, 2009, 60.
3. K. d. L. Harpe and B. Kohler, *J Phys Chem Lett*, 2011, 2, 133-138.
4. K. Kleinermanns, D. Nachtigallová and M. S. de Vries, *Int. Rev. Phys. Chem.*, 2013, 32, 308-342.
5. L. Serrano-Andrés, M. Merchán and A. C. Borin, *Chem. Eur. J.*, 2006, 12, 6559-6571.
6. W.-M. Kwok, C. Ma and D. L. Phillips, *J. Am. Chem. Soc.*, 2006, 128, 11894-11905.
7. H. Satzger, D. Townsend, M. Z. Zgierski, S. Patchkovskii, S. Ullrich and A. Stolow, *Proc. Natl. Acad. Sci.*, 2006, 103, 10196-10201.
8. D. Onidas, D. Markovitsi, S. Marguet and T. Gustavsson, *J. Phys. Chem. B*, 2002, 106, 11367.
9. P. R. Callis, *Annu. Rev. Phys. Chem.*, 1983, 34, 329-357.
10. J. Chen, A. K. Thazhathveetil, F. D. Lewis and B. Kohler, *J. Am. Chem. Soc.*, 2013, 135, 10290-10293.
11. A. S. Chatterley, C. W. West, G. M. Roberts, V. G. Stavros and J. R. R. Verlet, *J. Phys. Chem. Lett.*, 2014, 5, 843-848.
12. C. E. Crespo-Hernández, B. Cohen and B. Kohler, *Nature*, 2005, 436.
13. C. E. Crespo-HernÃndez and B. Kohler, *j. Phys. Chem. B.*, 2004, 108.
14. J. Eisinger, M. Guéron, R. G. Shulman and T. Yamane, *Proc. Natl. Acad. Sci.*, 1966, 55, 1015.
15. J. P. Ballini, M. Daniels and P. Vugny, *Biophys Chem*, 1991, 39.
16. B. Cohen, C. E. Crespo-Hernández, P. M. Hare and B. Kohler, *Ultrafast Molecular Events in Chemistry and Biology*, Martin, M. Hynes, J.T., Amsterdam, Elsevier edn., 2004.
17. C. E. Crespo-HernÃ¡ndez, K. De La Harpe and B. Kohler, *J. Am. Chem. Soc.*, 2008, 130.
18. R. Plessow, A. Brockhinke, W. Eimer and K. Kohse-Hoinghaus, *j. Phys. Chem. B*, 2000, 104.
19. J. Cadet and P. Vigny, eds., *Bioorganic Photochemestry*, Wiley, New York, 1990.
20. B. P. Ruzsicska and D. G. E. Lemaire, *CRC Handbook of Organic Photochemistry and Photobiology*, CRC, Boca Raton, 1995.
21. D. Markovitsi, A. Sharonov, D. Onidas and T. Gustavsson, *ChemPhysChem*, 2003, 4, 303-305.
22. P. Vigny and M. Duquesne, *Excited States of Biological Molecules*, New York, Wiley edn., 1976.
23. C. T. Middleton, K. de La Harpe, C. Su, Y. K. Law, C. E. Crespo-Hernández and B. Kohler, *Annu. Rev. Phys. Chem.*, 2009, 60.
24. C. E. Crespo-Hernández and B. Kohler, *J. Phys. Chem. B.*, 2004, 108.
25. C. E. Crespo-Hernández, B. Cohen and B. Kohler, *Nature*, 2006, 441, E8.
26. J. Chen and B. Kohler, *J. Am. Chem. Soc.*, 2014, 136, 6362-6372.
27. B. Cohen, C. E. Crespo-Hernández and B. Kohler, *Faraday Discuss.*, 2004, 127, 137 - 147.
28. T. Takaya, C. S, K. De La Harpe, C. E. Crespo-HernÃndez and B. Kohler, *Proc. Natl. Acad. Sci.*, 2008, 105.
29. C. T. Middleton, C. Su and B. Kohler, 2008.
30. J. M. L. Pecourt, J. Peon and B. Kohler, *J. Am. Chem. Soc.*, 2001, 123, 10370.
31. B. Cohen, P. M. Hare and B. Kohler, *J. Am. Chem. Soc.*, 2003, 125, 13594.
32. N. Ismail, L. Blancafort, M. Olivucci, B. Kohler and M. A. Robb, *J. Am. Chem. Soc.*, 2002, 124, 6818.
33. J. M. Pecourt, J. Peon and B. Kohler, *J. Am. Chem. Soc.* , 2000, 122.
34. C. Su, C. T. Middleton and B. Kohler, *J. Phys. Chem. B*, 2012, 116, 10266-10274.
35. M. C. Stuhldreier and F. Temps, *Faraday Discussions*, 2013, 163, 173-188.

36. I. Vayá, T. Gustavsson, F.-A. Miannay, T. Douki and D. Markovitsi, *J. Am. Chem. Soc.*, 2010, 132, 11834-11835.
37. A. Banyasz, I. Vayá, P. Changenet-Barret, T. Gustavsson, T. Douki and D. Markovitsi, *J. Am. Chem. Soc.,* 2011, 133, 5163-5165.
38. I. Vaya, T. Gustavsson, T. Douki, Y. Berlin and D. Markovitsi, *J. Am. Chem. Soc.*, 2012, 134, 11366-11368.
39. I. Buchvarov, Q. Wang, M. Raytchev, A. Trifonov and T. Fiebig, *Proc. Natl. Acad. Sci.*, 2007, 104.
40. N. K. Schwalb and F. Temps, *J. Am. Chem. Soc.*, 2007, 129, 9272-9273.
41. N. K. Schwalb and F. Temps, *Science*, 2008, 322, 243-245.
42. V. Sauri, J. P. Gobbo, J. J. Serrano-Pérez, M. Lundberg, P. B. Coto, L. Serrano-Andrés, A. C. Borin, R. Lindh, M. Merchán and D. Roca-Sanjuán, *J. Chem. Theory Comput.*, 2012, 9, 481-496.
43. J. P. Gobbo, V. Saurí, D. Roca-Sanjuán, L. Serrano-Andrés, M. Merchán and A. C. Borin, *J. Phys. Chem. B*, 2012, 116, 4089-4097.
44. S. Perun, A. L. Sobolewski and W. Domke, *J. Phys. Chem. A*, 2006, 110, 9031-9038.
45. A. L. Sobolewski, W. Domke and C. Hättig, *Proc. Natl. Acad. Sci.*, 2005, 102, 17903-17906.
46. D. Onidas, T. Gustavsson, E. Lazzarotto and D. Markovitsi, *J. Phys. Chem. B*, 2007, 111, 9644-9650.
47. D. Onidas, T. Gustavsson, E. Lazzarotto and D. Markovitsi, *Phys. Chem. Chem. Phys.*, 2007, 9, 5143–5148.
48. G. Olaso-González, M. Merchán and L. Serrano-Andrés, *J. Am. Chem. Soc.*, 2009, 131, 4368.
49. F. Santoro, V. Barone and R. Improta, *Proc. Natl. Acad. Sci.*, 2007, 104, 9931-9936.
50. F. Plasser and H. Lischka, *Photochem Photobiol Sci* 2013, 12, 1440-1452.
51. F. Santoro, V. Barone and R. Improta, *J. Am. Chem. Soc.*, 2009, 131, 15232-15245.
52. W. Zhang, S. Yuan, Z. Wang, Z. Qi, J. Zhao, Y. Dou and G. V. Lo, *Chemical Physics Letters*, 2011, 506, 303-308.
53. Y. Lu, Z. Lan and W. Thiel, *Angew. Chem. Int. Ed.*, 2011, 50, 6864-6867.
54. F. Plasser, A. J. A. Aquino, H. Lischka and D. Nachtigallova, *Topics in Current Chemistry*, 2014, DOI: 10.1007/128_2013_517.
55. F. Plasser, A. J. A. Aquino, W. L. Hase and H. Lischka, *J. Phys. Chem. A*, 2012, 116, 11151-11160.
56. V. A. Spata and S. Matsika, *J. Phys. Chem. A*, 2014, 118, 12021-12030; V. A. Spata and S. Matsika, *J. Phys. Chem. A*, 2013, 117, 8718-8728.
57. H. Yin, Y. MA, J. Mu, C. Liu and M. Rohlfing, *Phys. Rev. Lett.*, 2014, 112, 228301.
58. R. Improta, F. Santoro, V. Barone and A. Lami, *J Phys Chem A*, 2009, 113, 15346-15354.
59. R. Improta and V. Barone, *Angew. Chem. Int. Ed.*, 2011, 50, 12016-12019.
60. A. Banyasz, T. Gustavsson, D. Onidas, P. Changenet-Barret, D. Markovitsi and R. Improta, *Chem. Eur. J.*, 2013, 19, 3762-3774.
61. D. Markovitsi, D. Onidas, T. Gustavsson, F. Tablot and E. Lazzarotto, *J. Am. Chem. Soc.*, 2005, 127, 17130-17131.
62. D. Markovitsi, F. Tablot, T. Gustavsson, D. Onidas, E. Lazzarotto and S. Marguet, *Nature*, 2006, 441, E7.
63. F.-A. Miannay, A. Banyasz, T. Gustavsson and D. Markovitsi, *J. Am. Chem. Soc.*, 2007, 129, 14574.
64. E. Emanuele, K. Zakrzewska, D. Markovitsi, R. Lavery and P. Millié, *J. Phys. Chem. B*, 2005, 109, 16109–16118.
65. F. Plasser and H. Lischka, *Photochem. Photobiol. Sci.*, 2013, 12, 1440-1452.
66. I. Conti, P. Altoè, M. Stenta, M. Garavelli and G. Orlandi, *Phys. Chem. Chem. Phys.*, 2010, 12, 5016-5023.
67. I. Conti, M. Garavelli and G. Orlandi, *J. Am. Chem. Soc.*, 2009, 131, 16108-16118.
68. R. Chandrasekaran, A. Radha and H.-S. Park, *Acta Cryst. D* 1995, D51, 1025-1035
69. D. A. Case and e. al., *University of California, San Francisco CA*, 2004.
70. Y. Duan, C. Wu, S. Chowdhury, M. C. Lee, G. Xiong and e. al., *J. Comput. Chem.*, 2003, 24, 1999.
71. D. A. Case and e. al., *AMBER 12*, 2012.
72. H. Lin and D. G. Truhlar, *Theor. Chem. Acc.* , 2007, 117, 185.
73. P. Altoè, M. Stenta, A. Bottoni and M. Garavelli, *Theor. Chem. Acc.*, 2007, 118, 219.
74. M. L. Frisch and e. al., Gaussian Inc., Wallingford CT, 2004.
75. D. A. Case and e. al., *J. Comput. Chem.*, 2005, 26, 1668.
76. K. Andersson, P. Å. Malmqvist and B. O. Roos, *J. Chem. Phys*, 1992, 96, 1218.
77. F. Aquilante, T. B. Pedersen, V. Veryazov and R. Lindh, *Wiley Interdiscip. Rev. Comput. Mol. Sci.*, 2013, 3, 143-149.
78. F. Aquilante, L. D. Vico, N. Ferre, G. Ghigo, P. A. Malmqvist, P. Neogrady, T. B. Pedersen, M. Pitonak, M. Reiher, B. O. Roos, L. S. Andres, M. Urban, V. Veryazov, R. Lindh and *J. Comput. Chem.*, 2010, 31, 224-247.
79. M. Barbatti and H. Lischka, *J. Am. Chem. Soc.*, 2008, 130, 6831-6839.
80. S. Perun, A. L. Sobolewski and W. Domcke, *Chem. Phys.*, 2005, 313, 107.
81. W. C. Chung, Z. Lan, Y. Ohtsuki, N. Shimakura, W. Domcke and Y. Fujimura, *Phys. Chem. Chem. Phys.*, 2007, 9, 2075 - 2084.
82. A. L. Sobolewski and W. Domcke, *Eur. Phys. J. D*, 2002, 20, 369.
83. Y. Lei, S. Yuan, Y. Dou, Y. Wang and Z. Wen, *J. Phys Chem A*, 2008, 112, 8497-8504.
84. H. Chen and S. Li, *J. Phys. Chem. A*, 2005, 109, 8443.
85. S. Yamazaki and S. Kato, *J. Am. Chem. Soc.*, 2007, 129, 2901-2909.
86. L. Blancafort, *J. Am. Chem. Soc.*, 2006, 128, 210-219.
87. H. H. Ritze, H. Lippert, E. Samoylova, V. R. Smith, I. V. Hertel, W. Radloff and T. Schultz, *J. Chem. Phys.*, 2005, 122, 224320.
88. S. Perun, A. L. Sobolewski and W. Domcke, *J. Am. Chem. Soc.*, 2005, 127, 6257.
89. C. M. Marian, *J. Chem. Phys.*, 2005, 122, 104314.
90. L. Serrano-Andrés, M. Merchán and A. C. Borin, *Proc. Natl. Acad. Sci.*, 2006, 103, 8691-8696.
91. D. Nachtigallová, T. Zelený, M. Ruckenbauer, T. Müller, M. Barbatti, P. Hobza and H. Lischka, *J. Am. Chem. Soc.*, 2010, 132, 8261-8263.
92. N. J. Kim, G. Jeong, Y. S. Kim, J. Sung, S. K. Kim and Y. D. Park, *J. Chem. Phys.*, 2000, 113, 10051.
93. C. Ma, W. M. Kwok, W. S. Chan, P. Zuo, J. T. Wai Kan, P. H. Toy and D. L. Phillips, *J. Am. Chem. Soc.*, 2005, 127, 1463-1472.

94. B. Mennucci, A. Toniolo and J. Tomasi, *J. Phys. Chem. A*, 2001, 105, 4749.
95. N. J. Kim, H. Kang, G. Jeong, Y. S. Kim, K. T. Lee and S. K. Kim, *J. Phys. Chem.*, 2000, 104, 6552.
96. C. Plützer and K. Kleinermanns, *Phys. Chem. Chem. Phys.*, 2002, 4, 4877.
97. L. B. Clark, G. G. Peschel and I. Tinoco, *J. Am. Chem. Soc.*, 1965, 87, 11-15.
98. L. B. Clark, *J. Chem. Phys.*, 1990, 94, 2873-2879.
99. B. O. Roos, K. Andersson, M. P. Fulscher, P. A. Malmqvist, L. Serrano-Andres, K. Pierloot and M. Merchan, *Adv. Chem. Phys.*, 1996, 93, 219-331.
100. Y. Lee, M. Schmitt, K. Kleinermanns and B. Kim, *J. Phys. Chem. A*, 2006, 110, 11819-11823.
101. I. Conti, E. Di Donato, F. Negri and G. Orlandi, *J. Phys. Chem. A*, 2009, 113, 15265..

